Operator splitting algorithm for isokinetic SLLOD molecular dynamics

Guoai Pan, James F. Ely,[a] and Clare McCabe[b]
Chemical Engineering Department, Colorado School of Mines, Golden, Colorado 80401

Dennis J. Isbister
School of Physical, Environmental and Mathematical Science, University of New South Wales, Australian Defence Force Academy, Canberra, ACT 2600, Australia

(Received 21 October 2004; accepted 21 December 2004; published online 2 March 2005)

We apply an operator splitting method to develop a simulation algorithm that has complete analytical solutions for the Gaussian thermostated SLLOD equations of motion [D. J. Evans and G. P. Morriss, Phys. Rev. A **30**, 1528 (1984)] for a system under shear. This leads to a homogeneous algorithm for performing both equilibrium and nonequilibrium isokinetic molecular dynamics simulation. The resulting algorithm is computationally efficient. In particular, larger integration time steps can be used compared to simulations with regular Gaussian thermostated SLLOD equations of motion. The utility and accuracy of the algorithm are demonstrated through application to the Weeks–Chandler–Anderson fluid. Although strict conservation of the kinetic energy suppresses thermal fluctuations in the system, this algorithm does not allow simulations at lower shear rates than those normally afforded by older nonequilibrium molecular dynamics simulations. © *2005 American Institute of Physics*. [DOI: 10.1063/1.1858861]

I. INTRODUCTION

Molecular dynamics (MD) simulations have become a powerful tool with which to investigate the transport properties of liquids. In particular, both equilibrium and nonequilibrium molecular dynamics methods have been widely used in simulation work to study the diffusion, viscosity, and heat conductivity of model fluids. As a result of the increasing complexity and size of the systems being studied, significant effort has been devoted to developing efficient numerical algorithms to integrate the equations of motion. These range from the general-purpose ordinary differential equation solvers to the more recent symplectic numerical integrators.[1–8] For Hamiltonian systems, such as the conventional microcanonical (*N-V-E*) ensemble, there are explicit symplectic integrators (such as the Verlet algorithms) for use in MD simulations, which are stable, efficient, phase space area preserving, and time reversible. For non-Hamiltonian systems, "extended phase space" or "extended systems" are used to generate nonmicrocanonical ensembles such as the canonical (*N-V-T*), isothermal-isobaric (*N-P-T*), and isokinetic ensembles. For driven or constrained systems, a similar idea of extended systems can be used to derive symplectic-like integrators. Martyna *et al.*[6] reported comprehensive derivations of explicit, reversible integrators for extended systems of canonical and isothermal-isobaric ensembles. Tuckerman and co-workers[9,10] laid the statistical mechanical foundation for numerical integrators for use in non-Hamiltonian systems by generalizing results for Hamiltonian systems. Such integrators have been applied to the molecular dynamics simulation of a number of different systems, from simple model fluids to complex fluids involving, for example, internal restraints, disparate masses, and long-range forces. Furthermore, application of multiple-time-step techniques such as the Verlet/rRESPA algorithm has provided great success in the simulation of atomistically detailed models, where the fast internal motions of the atoms can be separated from the intermolecular interactions.[11,12]

In MD simulations generally a Nosé–Hoover[13–15] or Gaussian thermostat[16] is used to control the system's temperature, which generates canonical or isokinetic ensembles, respectively. The Nosé–Hoover thermostat allows the temperature to fluctuate and therefore describes a true canonical ensemble. However, the Gaussian thermostat, which originates from the idea of Gauss' principle of least constraint,[16] provides an isokinetic energy simulation, which keeps the average kinetic energy per particle rigorously constant and suppresses the fluctuations. Thus the isokinetic scheme produces the canonical ensemble distribution in coordinate space and yields the correct canonical ensemble averages for all properties that depend only on the positions of the particles,[9,14,16] but the thermal fluctuations are suppressed. An advantage of using the Gaussian thermostat over the Nosé–Hoover method is that one does not have to predetermine a relaxation time.

The Gaussian thermostated SLLOD equations[16] of motion for particle *i* being simulated in planar Couette flow are given by Eq. (1):

$$\frac{d\mathbf{r}_i}{dt} = \frac{\mathbf{p}_i}{m_i} + \dot{\gamma} y_i \hat{\mathbf{x}},$$

$$\frac{d\mathbf{p}_i}{dt} = \mathbf{F}_i - \dot{\gamma} p_{y,i} \hat{\mathbf{x}} - \alpha \mathbf{p}_i, \tag{1}$$

[a]Author to whom correspondence should be addressed. Fax: 303-273-3730. Electronic mail: jely@mines.edu
[b]Permanent address: Department of Chemical Engineering, Vanderbilt University, Nashville, TN 37235.

$$\frac{d}{dt}d_x(t) = \dot{\gamma},$$

where $\mathbf{r}=(x,y,z)$ and $\mathbf{p}=(p_x,p_y,p_z)$ denote the positions and momenta of the particles in phase space, $\dot{\gamma}$ is the shear rate, d_x is the lattice strain associated with the Lees–Edwards periodic boundary conditions[16] adopted in the simulation, $\hat{\mathbf{x}}$ is a unit vector in the x direction, and F_i is the force acting on particle i. α is the Gaussian thermostat multiplier used to fix the kinetic energy at each time step along the trajectory. It is easily shown that α is given at each time step by

$$\alpha = \frac{\sum_i \left(\mathbf{F}_i \cdot \frac{\mathbf{p}_i}{m_i} - \dot{\gamma} p_{x,i} p_{y,i}/m_i \right)}{\sum_i \frac{\mathbf{p}_i^2}{m_i}}. \tag{2}$$

Since α depends on both the forces and momenta of the particles, energy drifts when a conventional integrator is used to integrate the Gaussian thermostated SLLOD equations. To offset this effect, additional measures, such as an *ad hoc* rescaling of the velocities or incorporating an additional feedback term, have to be used to prevent the energy from drifting.[17]

In an effort to eliminate the need for *ad hoc* velocity scaling, Zhang[7] used operator splitting to develop a near-symplectic integrator for isokinetic equilibrium MD simulation that is easy to program, time reversible, and kinetic energy conserving. The equations of motion are split into equations involving changing vector fields of only the positions or momenta of the particles. For the latter, the force is constrained with the Gaussian thermostat multiplier. Through this operator splitting technique the equations for both vector fields can be solved exactly, which ensures the conservation of kinetic energy at each step in the time simulation and therefore eliminates any temperature drift. A similar strategy[8] has been applied to the Gaussian thermostated SLLOD equations for nonequilibrium systems. In this non-Hamiltonian system, since the shear field couples with the momenta, analytical solution of the differential equations for momenta was not possible and numerical solutions were used. Several iterative schemes were tested to solve the momentum equations of motion and they demonstrated the accuracy and stability of the operator splitting integrators.[8]

In this work the analytical algorithm originally due to Martyna[18] is presented, which is applicable to simulations[8] of both equilibrium and nonequilibrium (SLLOD) Gaussian thermostated systems. As in the equilibrium and nonequilibrium operator splitting methods, this algorithm developed by Martyna[18] controls the temperature remarkably well. We test the efficiency of this algorithm by using larger time steps compared to regular Gaussian thermostated SLLOD, as well as testing the lower strain rate regime in nonequilibrium molecular dynamics (NEMD). We proceed as follows: the composite algorithm of Zhang's version of the Martyna form of the algorithm will be presented as a homogeneous algorithm for both EMD and NEMD in Sec. II. In Sec. III, details of the simulations performed with the algorithm for the Weeks–Chandler–Anderson (WCA) fluid are given and the simulation results are presented in Sec. IV.

II. OPERATOR SPLITTING INTEGRATOR

Given the equations of motion, any phase space trajectory can be described by a time propagator based on the Liouville operator $iL=\dot{\Gamma}\cdot(\partial/\partial\Gamma)$ of the system where $\Gamma=(\mathbf{r},\mathbf{p})$. Starting with an initial state $\Gamma(0)=[\mathbf{r}(0),\mathbf{p}(0)]$, the state of the system at time t is given by

$$\Gamma(t) = \exp(iLt)\Gamma(0). \tag{3}$$

The time propagator of the phase space trajectory can be approximated by the noncommuting subpropagators through a factorization of the type,

$$\begin{aligned}\exp(iL\Delta t) &= \exp[(iL_1 + iL_2)\Delta t] \\ &= \exp\left(\frac{\Delta t}{2} iL_1\right)\exp(\Delta t iL_2)\exp\left(\frac{\Delta t}{2} iL_1\right) \\ &\quad + O(\Delta t^3),\end{aligned} \tag{4}$$

which is known as a second-order symmetrized Trotter factorization[19] with error of $O(\Delta t^3)$. The Liouville operator for the Gaussian thermostated SLLOD equations of motions (1) is given by

$$\begin{aligned}iL &= \sum_i \dot{\mathbf{r}}_i \cdot \frac{\partial}{\partial \mathbf{r}_i} + \sum_i \dot{\mathbf{p}}_i \cdot \frac{\partial}{\partial \mathbf{p}_i} + \dot{d}_x \cdot \frac{\partial}{\partial d_x} \\ &= \sum_i \frac{\mathbf{p}_i}{m_i} \cdot \frac{\partial}{\partial \mathbf{r}_i} + \dot{\gamma}\sum_i y_i \cdot \frac{\partial}{\partial x_i} + \sum_i \mathbf{F}_i \cdot \frac{\partial}{\partial \mathbf{p}_i} \\ &\quad - \dot{\gamma}\sum_i p_{y_i} \cdot \frac{\partial}{\partial p_{x_i}} - \alpha\sum_i \mathbf{p}_i \cdot \frac{\partial}{\partial \mathbf{p}_i} + \dot{\gamma} \cdot \frac{\partial}{\partial d_x}.\end{aligned} \tag{5}$$

This operator can be decomposed into a position operator iL_A and a momentum operator iL_B as

$$iL = iL_A + iL_B, \tag{6}$$

where

$$\begin{aligned}iL_A &= \sum_i \dot{\mathbf{r}}_i \cdot \frac{\partial}{\partial \mathbf{r}_i} + \dot{d}_x \cdot \frac{\partial}{\partial d_x} \\ &= \sum_i \frac{\mathbf{p}_i}{m_i} \cdot \frac{\partial}{\partial \mathbf{r}_i} + \dot{\gamma}\sum_i y_i \cdot \frac{\partial}{\partial x_i} + \dot{d}_x \cdot \frac{\partial}{\partial d_x},\end{aligned} \tag{7}$$

$$\begin{aligned}iL_B &= \sum_i \dot{\mathbf{p}}_i \cdot \frac{\partial}{\partial \mathbf{p}_i} \\ &= \sum_i \mathbf{F}_i \cdot \frac{\partial}{\partial \mathbf{p}_i} - \dot{\gamma}\sum_i y_i \cdot \frac{\partial}{\partial p_{x,i}} - \alpha\sum_i \mathbf{p}_i \cdot \frac{\partial}{\partial \mathbf{p}_i}.\end{aligned} \tag{8}$$

To order Δt^3, the second-order Trotter factorization in Eq. (4) allows two types of time propagators [denoted by $U(\Delta t)$] *ABA* and *BAB* to be generated

$$U(\Delta t) = \exp\left(\frac{\Delta t}{2}\mathbf{A}\cdot\frac{\partial}{\partial\Gamma}\right)\exp\left(\Delta t\mathbf{B}\cdot\frac{\partial}{\partial\Gamma}\right)\exp\left(\frac{\Delta t}{2}\mathbf{A}\cdot\frac{\partial}{\partial\Gamma}\right), \tag{9}$$

TABLE I. Simulation values of the reduced pressure, mean energy per particle, shear viscosity, and out-of-plane and in-plane viscosities at different shear rates for 256 particles and time step of 0.003. Steps are listed in millions. Figures in parentheses are the statistical uncertainties in the last digits.

$\dot{\gamma}$	Δt^*	*Nts*	P^*	E^*/N	$\eta(\dot{\gamma})$	η_-	η_0
0.0010	0.003	100	6.3787(19)	1.801 13(3)	2.28(18)	−1.99(16)	−3.88(10)
0.0100	0.003	30	6.3789(2)	1.801 18(3)	2.36(18)	−0.25(16)	−0.37(19)
0.0200	0.003	15	3.3796(5)	1.801 27(7)	2.31(2)	−0.05(2)	−0.15(3)
0.0400	0.003	14	6.3820(5)	1.801 62(7)	2.321(13)	−0.032(11)	−0.090(13)
0.0625	0.003	13	6.3861(5)	1.802 26(8)	2.300(9)	−0.015(7)	−0.052(9)
0.0900	0.003	12	6.3927(5)	1.803 24(8)	2.282(6)	0.005(5)	−0.016(6)
0.1225	0.003	11	6.4039(5)	1.804 93(8)	2.275(5)	0.021(4)	−0.003(5)
0.1600	0.003	10	6.4209(6)	1.807 47(9)	2.235(4)	0.037(3)	0.014(4)
0.2025	0.003	9	6.4419(6)	1.810 71(98)	2.205(3)	0.047(3)	0.023(3)
0.2500	0.003	8	6.4690(7)	1.814 83(10)	2.165(3)	0.067(2)	0.024(3)
0.3600	0.003	7	6.5439(7)	1.826 38(12)	2.095(2)	0.0885(17)	0.028(2)
0.4900	0.003	6	6.6415(8)	1.841 81(13)	2.009(2)	0.1093(14)	0.0306(16)
0.6400	0.003	5	6.7685(10)	1.862 18(16)	1.937(1)	0.1341(13)	0.0265(15)
0.8100	0.003	4	6.9310(11)	1.888 86(18)	1.871(1)	0.1524(11)	0.0258(13)
1.0000	0.003	4	7.1273(13)	1.921 70(20)	1.809(1)	0.1706(9)	0.0238(11)

$$U(\Delta t) = \exp\left(\frac{\Delta t}{2}\mathbf{B}\cdot\frac{\partial}{\partial\Gamma}\right)\exp\left(\Delta t\mathbf{A}\cdot\frac{\partial}{\partial\Gamma}\right)\exp\left(\frac{\Delta t}{2}\mathbf{B}\cdot\frac{\partial}{\partial\Gamma}\right). \tag{10}$$

Considering that force evaluations take up most of the CPU time in a simulation, a time propagator which requires fewer force calculations would be preferred. Therefore, since force evaluation is done in step *B*, time the propagator *ABA* requires only one force evaluation and improves computational efficiency over the propagator of type *BAB*. The Liouville operators in Eqs. (7) and (8) correspond to vectors for position and momentum, respectively,

$$\mathbf{A}_i = \begin{pmatrix} \dot{\mathbf{r}}_i \\ \dot{\mathbf{p}}_i \\ \dot{d}_x \end{pmatrix} = \begin{pmatrix} \dfrac{\mathbf{p}_i}{m} + \hat{\mathbf{x}}\dot{\gamma}y_i \\ 0 \\ \dot{\gamma} \end{pmatrix} \tag{11}$$

and

$$\mathbf{B}_i = \begin{pmatrix} \dot{\mathbf{r}}_i \\ \dot{\mathbf{p}}_i \\ \dot{d}_x \end{pmatrix} = \begin{pmatrix} 0 \\ \mathbf{F}_i - \hat{\mathbf{x}}\dot{\gamma}p_{yi} - \alpha\mathbf{p}_i \\ 0 \end{pmatrix}. \tag{12}$$

Analytical solutions can be derived for the differential equations associated with vector **A** at fixed momenta as given below

$$\begin{aligned} x_i(t+\Delta t) &= x_i(t) + \Delta t\dot{\gamma}y_i(t), \\ y_i(t+\Delta t) &= y_i(t), \\ z_i(t+\Delta t) &= z_i(t), \\ d_x(t+\Delta t) &= d_x(t) + \Delta t\dot{\gamma}, \\ \mathbf{p}_i(t+\Delta t) &= \mathbf{p}_i(t), \end{aligned} \tag{13}$$

where *x*, *y*, and *z* are the coordinates of particles in a curvilinear coordinate system.

Due to the coupling of the shear rate $\dot{\gamma}$ and forces in the Gaussian thermostat multiplier α, an analytic solution to vector **B** can only be obtained when the strain rate vanishes, leading to the equilibrium Gaussian thermostated equations of motion as formulated by Zhang in 1997.[7] However, by using a further split on vector **B** as suggested by Martyna,[18] it is possible to derive an analytic solution for a set of reversible, kinetic energy conserving equations. In particular, **B** can be split to decouple the shear field and the forces: using $\mathbf{B}_1$ for the equations containing the shearing field

$$\begin{aligned} &\frac{d\mathbf{r}_i}{dt} = 0, \\ \mathbf{B}_1:&\frac{d\mathbf{p}_i}{dt} = -\dot{\gamma}p_{yi}\hat{\mathbf{x}} - \alpha_1\mathbf{p}_i, \\ &\frac{d}{dt}d_x = 0, \end{aligned} \tag{14}$$

where

$$\alpha_1 = \frac{-\sum_i \dot{\gamma}p_{xi}p_{yi}/m_i}{\sum_i \mathbf{p}_i^2/m_i} \tag{15}$$

and $\mathbf{B}_2$ for the equations containing the forces

$$\begin{aligned} &\frac{d\mathbf{r}_i}{dt} = 0, \\ \mathbf{B}_2:&\frac{d\mathbf{p}_i}{dt} = \mathbf{F}_i - \alpha_2\mathbf{p}_i, \\ &\frac{d}{dt}d_x = 0, \end{aligned} \tag{16}$$

where

TABLE II. Simulation values of the reduced pressure, mean energy per particle, shear viscosity, and out-of-plane and in-plane viscosities at different shear rates for 2048 particles and various time-step sizes. Figures in parentheses are the statistical uncertainties in the last digits.

$\dot{\gamma}$	Δt^*	*Nts*	P^*	E^*/N	$\eta(\dot{\gamma})$	η_-	η_0
0.0010	0.003	100	6.390 70(7)	1.807 57(1)	2.331(7)	0.005(6)	0.000(7)
	0.01	200	6.394 86(3)	1.808 76(1)	2.32(3)	0.02(2)	0.00(3)
	0.02	100	6.408 47(1)	1.812 79(1)	2.398(12)	0.024(12)	−0.007(13)
0.0100	0.01	60	6.394 96(5)	1.808 78(1)	2.331(5)	0.011(4)	0.000(5)
	0.02	30	6.408 67(5)	1.812 82(1)	2.351(5)	−0.002(4)	0.008(5)
0.0200	0.003	30	6.391 10(12)	1.807 64(2)	2.330(6)	0.005(8)	0.008(6)
	0.01	18	6.395 73(8)	1.808 89(1)	2.334(5)	0.007(4)	0.001(5)
	0.02	18	6.409 27(6)	1.812 90(1)	2.350(3)	0.009(3)	0.006(3)
0.0400	0.02	16	6.411 50(6)	1.813 24(1)	2.3490(16)	0.0106(14)	0.010 0(17)
0.0625	0.003	20	6.397 87(15)	1.808 66(2)	2.308(2)	0.023(2)	0.016(3)
	0.01	14	6.402 02(10)	1.809 84(2)	2.3182(15)	0.0188(13)	0.016 9(15)
	0.02	14	6.415 87(7)	1.813 90(1)	2.3396(11)	0.0186(10)	0.014 0(11)
0.0900	0.02	12	6.423 26(7)	1.815 01(1)	2.3219(9)	0.0276(8)	0.021 6(9)
0.1225	0.003	10	6.416 2(2)	1.811 42(3)	2.2725(17)	0.0386(15)	0.026 5(18)
	0.01	10	6.420 52(11)	1.812 63(2)	2.2769(10)	0.0377(8)	0.027 0(10)
	0.02	10	6.434 84(8)	1.816 77(1)	2.2988(7)	0.0379(6)	0.026 9(7)
0.1600	0.02	9	6.451 32(9)	1.819 27(1)	2.2693(6)	0.0487(5)	0.032 4(6)
0.2025	0.003	9	6.453 9(2)	1.817 15(3)	2.2083(11)	0.0582(10)	0.035 0(11)
	0.01	9	6.458 39(12)	1.818 39(2)	2.2142(6)	0.0583(5)	0.035 3(7)
	0.02	9	6.473 24(9)	1.822 62(1)	2.2338(4)	0.0584(4)	0.034 8(4)
0.2500	0.02	8	6.500 94(9)	1.826 87(1)	2.1953(4)	0.0699(3)	0.037 5(4)
0.3600	0.003	7	6.653 9(3)	1.832 59(4)	2.0913(7)	0.0903(6)	0.037 8(8)
	0.01	7	6.559 04(15)	1.833 96(2)	2.0954(4)	0.0892(3)	0.039 3(4)
	0.02	7	6.575 06(10)	1.838 39(2)	2.1128(3)	0.0907(2)	0.038 9(3)
0.4900	0.02	6	6.675 49(11)	1.854 27(2)	2.0315(2)	0.1123(2)	0.037 4(2)
0.6400	0.003	5	6.780 1(3)	1.868 73(5)	1.9376(5)	0.1301(4)	0.032 7(5)
	0.01	5	6.786 00(19)	1.870 22(3)	1.9416(3)	0.1306(2)	0.032 8(3)
	0.02	5	6.804 91(14)	1.875 17(2)	1.9562(2)	0.1324(2)	0.032 9(2)
0.8100	0.02	4	6.966 94(16)	1.901 88(3)	1.8878(2)	0.1521(1)	0.027 3(2)
1.0000	0.003	4	7.137 3(5)	1.928 06(7)	1.8089(4)	0.1685(3)	0.022 0(4)
	0.01	4	7.143 9(3)	1.929 72(4)	1.8121(2)	0.1686(17)	0.022 4(2)
	0.02	4	7.166 20(17)	1.935 37(3)	1.8251(2)	0.1707(1)	0.022 32(16)

$$\alpha_2 = \frac{\sum_i \mathbf{F}_i \cdot \mathbf{p}_i/m_i}{\sum_i \mathbf{p}_i^2/m_i}. \tag{17}$$

In the splitting of vector **B**, Gauss' principle of least constraint is applied in both $\mathbf{B}_1$ and $\mathbf{B}_2$ to ensure kinetic energy conservation in each substep of integration. Thus, in all steps of the integration (i.e., solving **A**, $\mathbf{B}_1$, and $\mathbf{B}_2$), the kinetic energy is conserved and fixed. Analytic solutions for the equations of motion associated with vector $\mathbf{B}_1$ and $\mathbf{B}_2$. For $\mathbf{B}_1$

$$\mathbf{r}_i(t+\Delta t) = \mathbf{r}_i(t),$$

$$\mathbf{p}_i(t+\Delta t) = g(\Delta t)[\mathbf{p}_i(t) - \hat{\mathbf{x}}\Delta t\dot{\gamma}p_{yi}(t)], \tag{18}$$

$$d_x(t+\Delta t) = d_x(t),$$

g is defined as

$$g(\Delta t) = \frac{1}{\sqrt{1 - 2c_1\Delta t + c_2\Delta t^2}}, \tag{19}$$

where

$$c_1 = \frac{\dot{\gamma}}{\sum_i \mathbf{p}_i^2/m_i}\sum_i p_{xi}(t)p_{yi}(t)/m_i \tag{20}$$

and

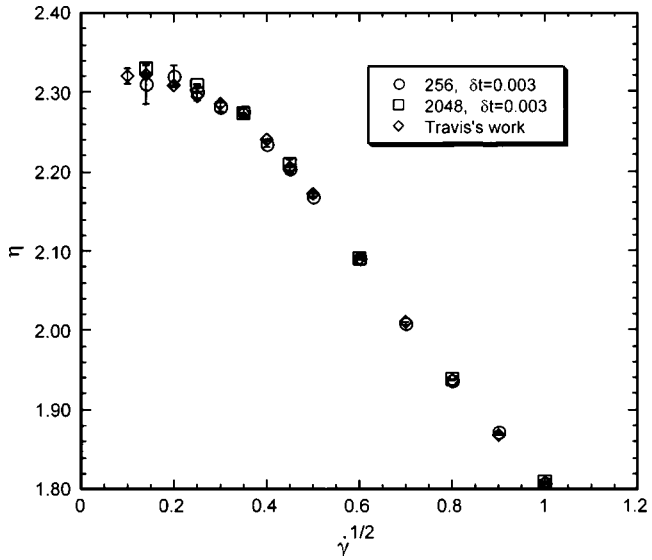

FIG. 1. Shear viscosity vs square root of shear rate $\dot{\gamma}^{1/2}$. Simulations use the same step size 0.003. Open circles and squares are symbols for system of 256 particles and 2048 particles using the operator splitting algorithm. Open diamond symbols are data points from Travis's work (Ref. 20).

$$c_2 = \frac{\dot{\gamma}^2}{\sum_i \mathbf{p}_i^2/m_i} \sum_i p_{yi}(t) p_{yi}(t)/m_i. \tag{21}$$

Similarly, solutions for $\mathbf{B}_2$ are given by

$$\mathbf{r}_i(t+\Delta t) = \mathbf{r}_i(t),$$

$$\mathbf{p}_i(t+\Delta t) = \frac{1-h}{e(\Delta t) - h/e(\Delta t)} \times \left[\mathbf{p}_i(t) - \mathbf{F}_i(t) \frac{1+h-e(\Delta t)-h/e(\Delta t)}{(1-h)\beta} \right], \tag{22}$$

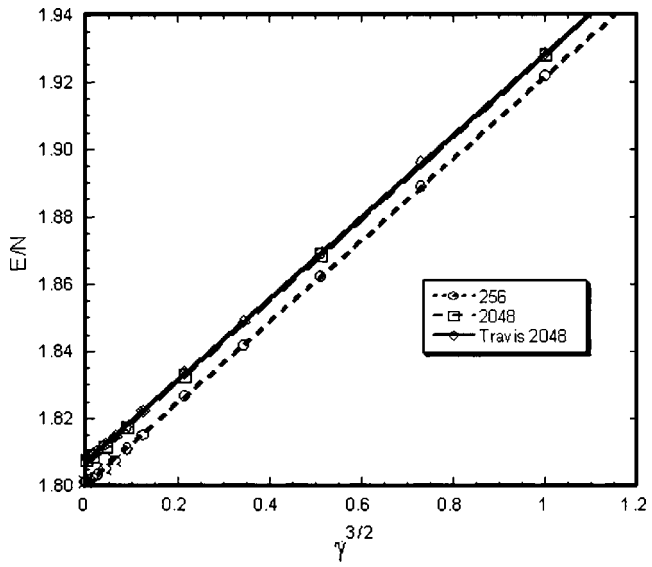

FIG. 2. Simulated energy per particle in systems of different sizes with a time-step size of 0.003 as a function of $\dot{\gamma}^{3/2}$. Open circles and squares are data points from system of 256 and 2048 particles, respectively, obtained using the developed algorithm. Open diamonds are data points from Ref. 20. The lines are the linear fits of the data points with respect to $\dot{\gamma}^{3/2}$ and error bars are too small to be shown.

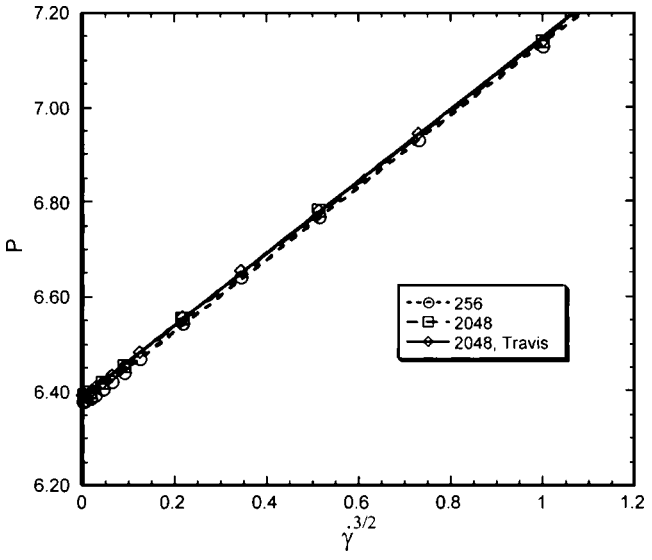

FIG. 3. Hydrostatic pressure vs $\dot{\gamma}^{3/2}$ in different sized systems using a reduced simulation time step size of 0.003. Open circles and squares are data points from system of 256 and 2048 obtained using the developed algorithm. Open diamonds are from Ref. 20. The lines are linear least-squares fits with respect to $\dot{\gamma}^{3/2}$.

$$d_x(t+\Delta t) = d_x(t),$$

where e, β, and h are defined as

$$e(\Delta t) = \exp(-\beta \Delta t), \tag{23}$$

$$\beta = \sqrt{\frac{\sum_i \mathbf{F}_i \cdot \mathbf{F}_i/m_i}{\sum_i \mathbf{p}_i^2/m_i}}, \tag{24}$$

and

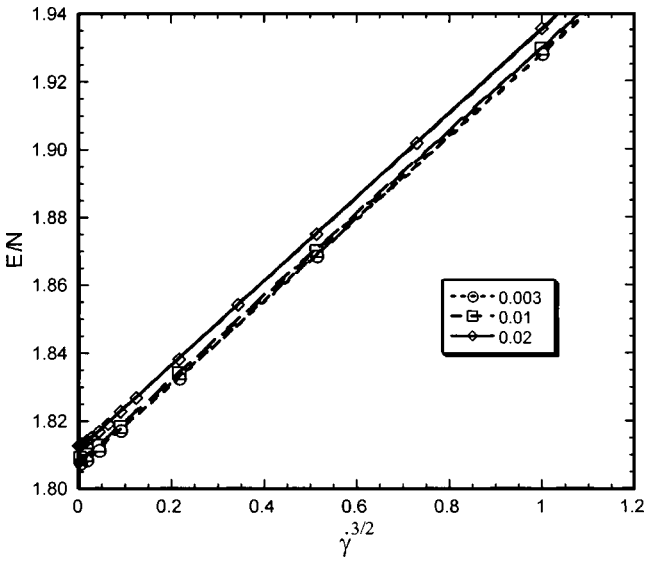

FIG. 4. Simulation time-step size effect on hydrostatic pressure in a system of 2048 particles. Open circles are from simulations using a time-step size of 0.003, open squares from those of 0.01, and open diamonds from those of 0.02. The lines are linear least-squares fit with respect to $\dot{\gamma}^{3/2}$.

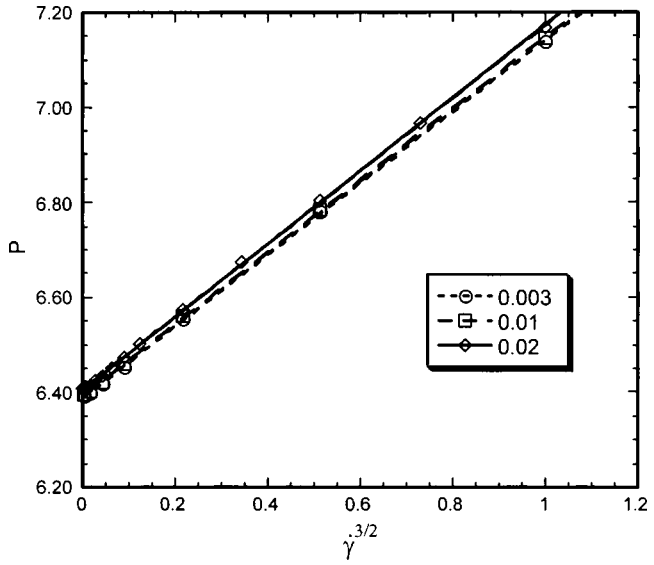

FIG. 5. Energy simulations for 2048 particles using different time-step sizes. The open circles are from simulations of step size 0.003, open squares from step size 0.01, and open diamonds from step size 0.02. The lines are linear fit curves of the data points with respect to $\dot{\gamma}^{3/2}$. The error bars are too small to be displayed.

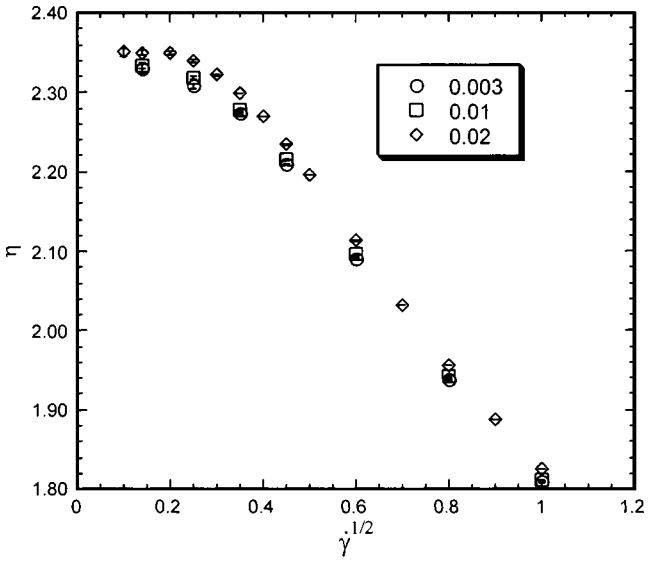

FIG. 6. Simulated shear viscosities as a function of $\dot{\gamma}^{1/2}$ in a 2048 particle system using the proposed algorithm with different time-step sizes 0.003, 0.01, and 0.02. The error bars are shown in the figures, which are small.

$$h = \frac{\alpha(t) + \beta}{\alpha(t) - \beta}, \tag{25}$$

where

$$\alpha(t) = \frac{\sum_i \mathbf{f}_i \cdot \mathbf{p}_i / m_i}{\sum_i \mathbf{p}_i^2 / m_i}. \tag{26}$$

The time propagator $\mathbf{AB}_1\mathbf{B}_2\mathbf{B}_1\mathbf{A}$ can be generated through a second-order Trotter factorization with a single force evaluation in the $\mathbf{B}_2$ step. Formally this set of steps is written as

$$U(\Delta t) = \exp\left(\frac{\Delta t}{2}\mathbf{A} \cdot \frac{\partial}{\partial \Gamma}\right)\exp\left(\frac{\Delta t}{2}\mathbf{B}_1 \cdot \frac{\partial}{\partial \Gamma}\right)\exp\left(\Delta t \mathbf{B}_2 \cdot \frac{\partial}{\partial \Gamma}\right) \times \exp\left(\frac{\Delta t}{2}\mathbf{B}_1 \cdot \frac{\partial}{\partial \Gamma}\right)\exp\left(\frac{\Delta t}{2}\mathbf{A} \cdot \frac{\partial}{\partial \Gamma}\right). \tag{27}$$

In each substep of the integration the kinetic energy is strictly conserved and due to the exact analytical solutions provided for each operator, kinetic energy drift will not occur during a particular time step, at least to $O(\Delta t)^3$. Since the force evaluation is required only once in the operator $\mathbf{B}_2$, the operator splitting approach of $\mathbf{AB}_1\mathbf{B}_2\mathbf{B}_1\mathbf{A}$ minimizes CPU time accordingly. For an equilibrium MD simulation in which no flow field is present, the operator $\mathbf{B}_1$ vanishes and the operator splitting algorithm for kinetic energy conserving equilibrium simulation is recovered.[7]

To summarize, the algorithm provides a homogeneous scheme that can be used to perform kinetic energy conserving MD simulations that is explicit and time reversible. Additionally, it is computational efficient, less memory demanding, and as we shall show in the results section, allows for larger integrating time steps compared to conventional integrators.

TABLE III. Linear least-squares fit coefficients of internal energy and hydrostatic pressure for systems of different sizes and different simulation time-step sizes. Energy is fit as $E(\gamma)/N = E_0 + E_1\gamma^{3/2}$ and pressure is fit as $P(\gamma) = P_0 + P_1\gamma^{3/2}$. Uncertainties in the last digit are given in parentheses.

Simulation	Δt^*	E_0	E_1	P_0	P_1
256	0.003	1.8003(2)	1.1212(5)	6.376(1)	0.758(3)
2048	0.003	1.8066(2)	1.1214(5)	6.388(2)	0.753(5)
	0.01	1.8078(2)	1.1219(5)	6.392(2)	0.756(5)
	0.02	1.8120(2)	1.1233(4)	6.406(1)	0.767(3)
[a]		1.8074(1)	1.1212(4)	6.389(2)	0.756(4)

[a]Reference 20.

III. SIMULATION DETAILS

Travis and co-workers[20] have carried out extensive NEMD simulations on a WCA fluid[21] $[u(r) = 4(r^{-12} - r^{-6})$

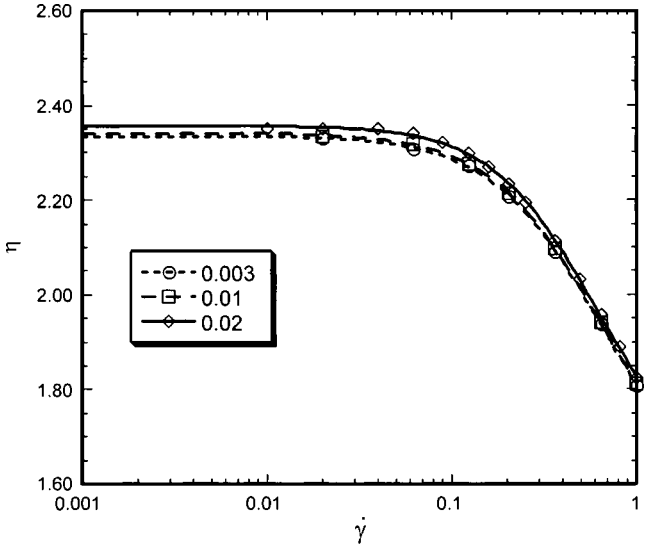

FIG. 7. The shear viscosities of WCA fluid of 2048 particles measured using different time-step sizes as a function of shear rate $\dot{\gamma}$. The open circle, square, and diamond symbols correspond to time step sizes 0.003, 0.01, and 0.02. The lines are fitted Cross model curves.

$+1, r \leqslant 2^{1/6}; u(r)=0, r>2^{1/6}]$ of 2048 particles using the Gaussian thermostated SLLOD equations of motion and explored the strain rate dependence of a range of rheological properties. In that work the WCA potential parameters ε and σ as well as the particle mass were set to be unity. The particle density was $\rho^*=0.8442$ and the temperature $T^*=0.722$. In this work we have deliberately chosen to study the same model fluid at the same density and temperature, but have simulated two systems consisting of 256 and 2048 particles in order to determine if any system size dependence is associated with the new algorithm. Also, different reduced time steps ranging from 0.003 to 0.02 were used in our simulations of the larger system to explore the limit of step size. In the NEMD simulations the viscosity of the fluid η is determined by measuring the pressure tensor during the simulation,

$$\eta = -\frac{\langle P_{xy} \rangle}{\dot{\gamma}}, \tag{28}$$

where P_{xy} is the xy element of the pressure tensor in coordinates with strain rate defined as $\dot{\gamma}=dv_x/dy$.

IV. RESULTS

The results of the NEMD simulations for 256 and 2048 particle systems are given in Tables I and II, respectively. The proposed algorithm is very stable and completely conserves kinetic energy during the simulations. This was demonstrated from a simulation of 256 particles at reduced shear rate 0.001 using a reduced time step of 0.02. During the simulation, the temperature deviation from the set value rose from 2.53×10^{-11} in the first 10^6 time steps to 1.39×10^{-9} in 10^8 time steps, all attributable to machine rounding errors.

The shear viscosities of the WCA fluid from simulations of 256 and 2048 particles using the new algorithm versus the square root of the shear rate are plotted in Fig. 1. For comparison we have also included the results of Travis, Searles, and Evans[20] for a time step of $\Delta t^*=0.003$. In Fig. 1, we see that to within their combined uncertainty, the data points from the new algorithm using either 256 or 2048 particles and the data of Travis, Searles, and Evans[20] fall on the same curve. The viscosities exhibit shear thinning behavior at high strain rates and there is a Newtonian plateau at low strain rates. Figures 2 and 3 compare our results with those of Ref. 20 for the mode coupling theory prediction that the hydrostatic pressure and internal energy per particle depend on the shear rate as $\dot{\gamma}^{3/2}$. Throughout this work the internal energy per particle was calculated as the sum of the WCA interactions divided by N. The internal energy per particle in the simulations performed with 2048 particles from the new algorithm show a very slight difference from those reported in Ref. 20.

Simulations of the 2048 particle system using larger time steps of 0.01 and 0.02 have also been performed to probe the efficiency and stability of the proposed algorithm as the time-step size is increased. Figures 4 and 5 show the effect of time-step size on our simulation results for the hydrostatic pressure and internal energy per particle. Linear least-squares fits of these results as functions of $\dot{\gamma}^{3/2}$ reproduce the data points very well for both the internal energy and the hydrostatic pressure and the fitted values of the coefficients are listed in Table III. However, the energy per particle shows a significant number dependence as can be seen from a comparison of the results for the systems of 256 and 2048 particles. A similar number dependence can be seen for the hydrostatic pressure (Fig. 3). Our simulations for 2048 particles using the new algorithm predict pressures that are in good agreement with the results of Ref. 20. A slight underprediction is observed for the pressure when simulating with 256 particles as compared with 2048 particles.

TABLE IV. The Cross model fit parameters for simulations with time-step size 0.003, 0.01, and 0.02.

Δt^*	$\eta(0)$	η_∞	K	m
0.003	2.336(3)	1.53(3)	1.56(9)	1.45(5)
0.01	2.342(4)	1.54(4)	1.6(1)	1.47(6)
0.02	2.357(2)	1.60(3)	1.70(8)	1.56(5)

The strain rate dependent viscosities for simulations with time steps of 0.003, 0.01, and 0.02 are plotted in Fig. 6 with respect to $\dot{\gamma}^{1/2}$ and in Fig. 7 with respect to $\dot{\gamma}$ on a log scale. While the viscosities using time steps 0.003 and 0.01 are very close to each other, deviations are observed for the largest reduced time step of 0.02. Figure 4 shows that a single square root functional form of strain rate, as suggested by the mode coupling theory[22] is not good enough to describe the viscosity dependence on strain rate $\gamma^{1/2}$. The viscosities are better fitted to the Cross model[23] given by Eq. (19) with four adjustable parameters, as shown in Fig. 5.

$$\frac{\eta(\dot{\gamma})-\eta_\infty}{\eta(0)-\eta_\infty} = \frac{1}{1+(K\dot{\gamma})^m}. \tag{29}$$

The parameters obtained in these fits are given in Table IV. We note that to within statistical uncertainty m can be taken to be 1.5 and that the values of $\eta(0)$ for the two smaller time steps (0.003 and 0.01) are statistically identical.

Normal stress differences are also of interest in studying the rheological behavior of fluids. The in-plane viscosity η_- and out-of-plane viscosity η_0 are defined in Eqs. (29) and (30):

$$\eta_- = -(P_{xx}-P_{yy})/2\dot{\gamma}, \tag{30}$$

$$\eta_0 = -\left[P_{zz}-\tfrac{1}{2}(P_{xx}+P_{yy})\right]/2\dot{\gamma}, \tag{31}$$

where P_{xx}, P_{yy}, and P_{zz} are the diagonal components of the pressure tensor which contribute to the transverse pressure component. The in-plane and out-of-plane viscosities are related to the normal stress differences, which are very difficult to measure accurately, particularly at low strain rates. From the data given in Tables I and II, we note that both the in-plane and out-of-plane viscosities show a strong number dependence. The in-plane viscosities for the different time-step sizes for 2048 particles are plotted in Fig. 8. The simulations using the new algorithm with step sizes 0.003, 0.01, and 0.02 all agree within the error range with each other and with Travis' work,[20] except at low strain rates. As the strain rate increases, the in-plane viscosity increases and then decreases

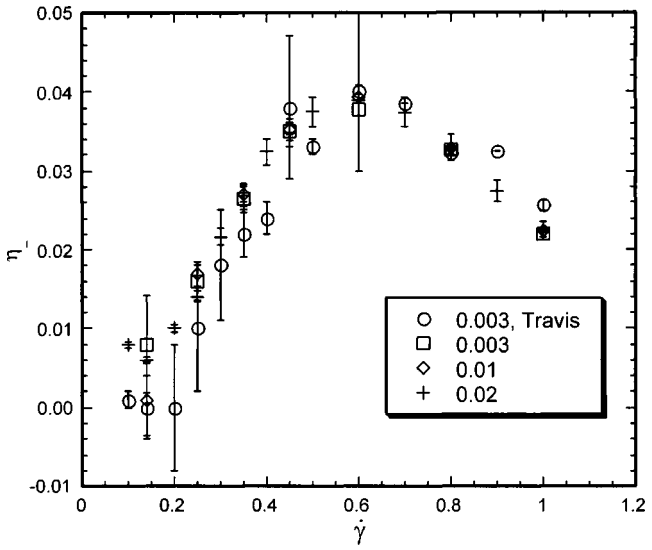

FIG. 8. In-plane viscosity as a function of shear rate $\dot{\gamma}$ for systems of 2048 particles using different time steps. Open circles are from Ref. 20. Open squares, diamonds, and crosses are simulations using the developed algorithm. Error bars are displayed.

at a reduced shear rate of around 0.5. The out-of-plane viscosities, shown for 2048 particles in Fig. 9, increase monotonically with the square root of the strain rate. Out-of-plane viscosity data points from Ref. 20 and the new algorithm using different time-step sizes again essentially fall on one master curve. The out-of-plane viscosity increases monotonically with strain rates, which can be fitted very well to the function given by

$$\eta_-(\dot{\gamma}) = \frac{a}{1 + b\dot{\gamma}}. \tag{32}$$

Due to the difficulty of measuring normal stress differences which result in values with relatively large error bars, the in-plane and out-of-plane viscosities are not as sensitive as the shear viscosities to step size, however, they show a very strong number dependence.

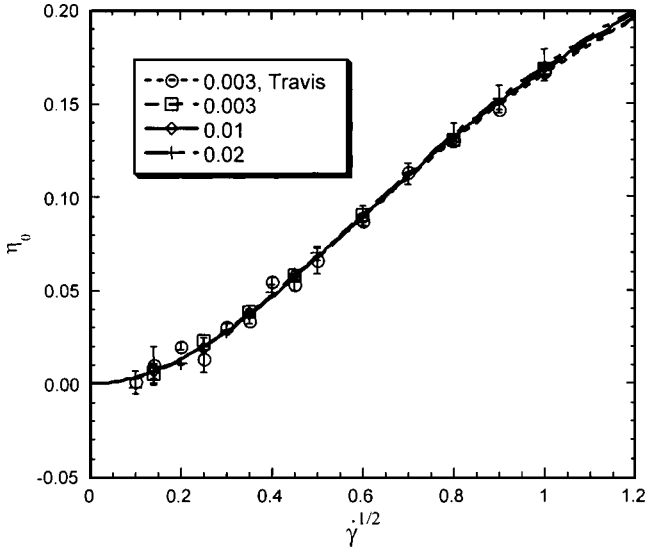

FIG. 9. The out-of-plane viscosity increases monotonically with $\dot{\gamma}^{1/2}$ for systems of 2048 particles using different time-step sizes. The open circles are from Ref. 20. The open squares, diamonds, and crosses are simulations using the developed algorithm with time-step sizes 0.003, 0.01, and 0.02. The curves are results of least squares fitting using Eq. (22).

V. CONCLUSION

We have used a homogeneous algorithm, the Zhang–Martyna (ZM) composite algorithm, for kinetic energy conserving simulations using the Gaussian thermostated equations of motion for both equilibrium[8] and SLLOD nonequilibrium dynamics.[18] In the algorithm the extended system Liouville operator is split in order to develop an analytic solution and Gauss' principle of least constraint is applied. This enables the temperature to be fixed at each substep of the operator manipulation, thus conserving the kinetic energy at each integration time step. Since the kinetic energy is strictly fixed, no drift in the temperature is observed, though a slight deviation is noted due to the accumulation of numerical errors by some other conventional integrators. In this sense, the new algorithm provides a way to realize the "genuine" isokinetic simulation of a SLLOD shearing system. With the new algorithm the evolution of each trajectory requires information on only the previous time state of phase space, and no empirical relaxation time is required for temperature control. This should make the algorithm very useful when accurate descriptions of transient states in simulations are required. For example, the new integrator should be ideal in transient time correlation function calculations.

The new operator splitting algorithm has been validated through a comprehensive comparison of the rheological properties obtained from NEMD simulations with those from Travis, Searles, and Evans.[20] At the same time-step size of 0.003, the algorithm predicts viscosities, energies per particle, and hydrostatic pressure in agreement with Travis's data. The stability of the integrator enables the adoption of larger reduced time steps in the simulation while retaining accurate results. The NEMD simulations with different time-step sizes demonstrate that the new algorithm can be used with reduced time-step size of 0.01 while it still gets accurate results as smaller time steps. We note, however, that the ZM algorithm was not capable of accurately extending current NEMD simulations to extremely low shear rates (i.e., less than 0.001) found on the Newtonian plateau: it simply failed in this sensitive yet important test of numerical integration of NEMD for very low shear rate cases.

ACKNOWLEDGMENTS

C.M.C. and G.P. acknowledge the donors of the American Chemical Society Petroleum Research Fund for support of this research. J.F.E. acknowledges the support of the Department of Energy, Office of Science, Grant No. DE-FG03-95ER14568.

[1] J. Suzuki, J. Math. Phys. **26**, 601 (1985).
[2] H. Yoshida, Phys. Lett. A **150**, 262 (1990).
[3] H. Yoshida, Celest. Mech. Dyn. Astron. **56**, 27 (1993).
[4] M. Tuckerman, B. J. Berne, and G. J. Martyna, J. Chem. Phys. **97**, 1990 (1992).
[5] P. Saha and S. Tremaine, Astron. J. **104**, 1633 (1992).
[6] G. J. Martyna, M. E. Tuckerman, D. J. Tobias, and M. L. Klein, Mol. Phys. **87**, 1117 (1996).

[7]F. Zhang, J. Chem. Phys. **106**, 6102 (1997).
[8]F. Zhang, D. J. Searles, D. J. Evans, J. S. den Toom Hansen, and D. J. Isbister, J. Chem. Phys. **111**, 18 (1999).
[9]M. E. Tuckerman, C. J. Mundy, and G. J. Martyna, Europhys. Lett. **45**, 149 (1999).
[10]M. E. Tuckerman, Y. Liu, G. Ciccotti, and G. J. Martyna, J. Chem. Phys. **115**, 1678 (2001).
[11]C. J. Mundy, J. I. Siepmann, and M. L. Klein, J. Chem. Phys. **102**, 3376 (1995).
[12]S. T. Cui, P. T. Cummings, and H. D. Cochran, J. Chem. Phys. **104**, 255 (1996).
[13]S. Nosé, Mol. Phys. **52**, 255 (1984).
[14]S. Nosé, J. Chem. Phys. **81**, 511 (1984).
[15]W. G. Hoover, Phys. Rev. A **31**, 1695 (1985).
[16]D. J. Evans and G. P. Morriss, *Statistical Mechanics of Nonequilibrium Liquids* (Academic, New York, 1990).
[17]A. Baranyai and D. J. Evans, Mol. Phys. **70**, 53 (1990).
[18]G. J. Martyna (private communication).
[19]H. F. Trotter, Proc. Am. Math. Soc. **10**, 545 (1959).
[20]K. P. Travis, D. J. Searles, and D. J. Evans, Mol. Phys. **95**, 195 (1998).
[21]J. D. Weeks, D. Chandler, and H. C. Anderson, J. Chem. Phys. **54**, 5237 (1971).
[22]Y. Pomeau and P. Résibois, Phys. Rep., Phys. Lett. **19**, 63 (1975).
[23]M. M. Cross, J. Colloid Sci. **20**, 417 (1965).